

Anomalously High Phonon Thermal Conductivity Driven by Weak Electron-Phonon Coupling in Weyl Semimetals TaAs and TaP

Xianyong Ding,^{1,*} Xin Jin,^{1,*} Dengfeng Li,² Jing Fan,³ Peng Yu,¹ Xiaoyuan Zhou,⁴ Xiaolong Yang,^{4,5,†} and Rui Wang^{4,5,‡}

¹College of Physics and Electronic Engineering, Chongqing Normal University, Chongqing 401331, China

²School of Science, Chongqing University of Posts and Telecommunications, Chongqing, 400065, China

³Center for Computational Science and Engineering,

Southern University of Science and Technology, Shenzhen 518055, P. R. China

⁴College of Physics and Center of Quantum Materials and Devices,

Chongqing University, Chongqing 401331, China

⁵Chongqing Key Laboratory for Strongly Coupled Physics,
Chongqing University, Chongqing 401331, China

In conventional metals, thermal transport is governed by electrons, with phonon contributions often considered negligible. Here, through rigorous first-principles calculations, we uncover a phonon-dominated thermal transport regime in the Weyl semimetals TaAs and TaP. Remarkably, although TaP is metallic, its phonon thermal conductivity (κ_{ph}) reaches as high as 171 W/mK at room temperature, surpassing its electronic counterpart by more than a factor of five. This anomalously high κ_{ph} is enabled by the unique electronic and phononic band structures, characterized by the Weyl nodes near the Fermi level, together with acoustic phonon bunching and a wide frequency gap in the phonon spectrum, which collectively suppress phonon-electron and phonon-phonon scattering processes. Due to the substantial phonon contribution, the derived Lorenz number deviates strongly from the conventional Wiedemann-Franz law. We further show that the significance of phonon thermal transport is universal across topological semimetals. Our work provides deeper insight into thermal transport mechanisms in topological semimetals and extends the scope for discovering materials with high thermal conductivity.

Weyl semimetals (WSMs), known for hosting robust Weyl quasiparticles, have garnered significant attention in condensed matter physics and materials research [1–7]. Distinguished by their linear bulk band dispersion relations and the presence of robust Weyl points, WSMs exhibit a range of intriguing phenomena such as Fermi arc surface states [8, 9], high mobility [10], large unsaturated magnetic moments [11–13], negative magneto-resistance [14–16], and chiral anomaly [15, 17–19]. Among the prototypical WSMs, TaAs family (TaAs, TaP, NbAs, and NbP) has been well studied, with experiments directly confirming the existence of Weyl fermions and Fermi-arc surface states, thereby establishing its non-trivial topological nature [5–7, 15, 20]. While the electronic and topological properties of WSMs have been extensively explored, their thermal transport characteristics remain largely uncharted. Given its importance for both fundamental science and diverse applications, establishing a comprehensive understanding of heat conduction in such systems is imperative. Moreover, in Weyl semimetals, the linearly dispersing bands near the Fermi level typically lead to low carrier densities and consequently weak phonon-electron (ph-el) scattering [21–23], which facilitates an enhancement of the phonon contribution to thermal conductivity (κ_{ph}). These features suggest that WSMs may provide a promising materials platform for

achieving high thermal conductivity.

Conventionally, it has been held that in metallic systems, thermal transport is primarily carried by free electrons, with the contribution from phonons generally considered negligible. In such cases, the electronic thermal conductivity (κ_e) can be estimated from electrical conductivity (σ) via the Wiedemann-Franz law (WFL), expressed as $\kappa_e = L\sigma T$ [24]. Here, the Lorenz number L is commonly taken as the Sommerfeld value [25, 26], $L_0 = \pi^2 k_B^2 / 3e^2 = 2.445 \times 10^{-8} \text{ W}\Omega\text{K}^{-2}$. However, this picture may not hold in WSMs, where low carrier densities can lead to a severely limited κ_e , while weak ph-el scattering in combination with distinct phonon band structures may render the phonon contribution substantial or even dominant. Indeed, unusually large κ_{ph} have been reported in several systems, including W [27], Be [28], θ -TaN [22], and other [21, 29]. In these systems, heat transport is governed primarily by phonons rather than by charge carriers, contrasting sharply with conventional metallic behavior. For the TaAs family, weak ph-el scattering and low carrier densities are expected to amplify the role of phonon thermal transport. Concurrently, large cation-anion mass differences and strong covalent bonding also leads to a substantial frequency gap between acoustic and optical phonons (a-o gap) and bunching of acoustic branches [30], which strongly suppresses three-phonon (3ph) scattering processes. Collectively, these features point toward the TaAs family as a candidate system for exhibiting anomalously high phonon thermal conductivity.

In this letter, we present a systematic first-principles

* X. Y. D. and X. J. contributed equally to this work.

† yangxl@cqu.edu.cn

‡ rcwang@cqu.edu.cn

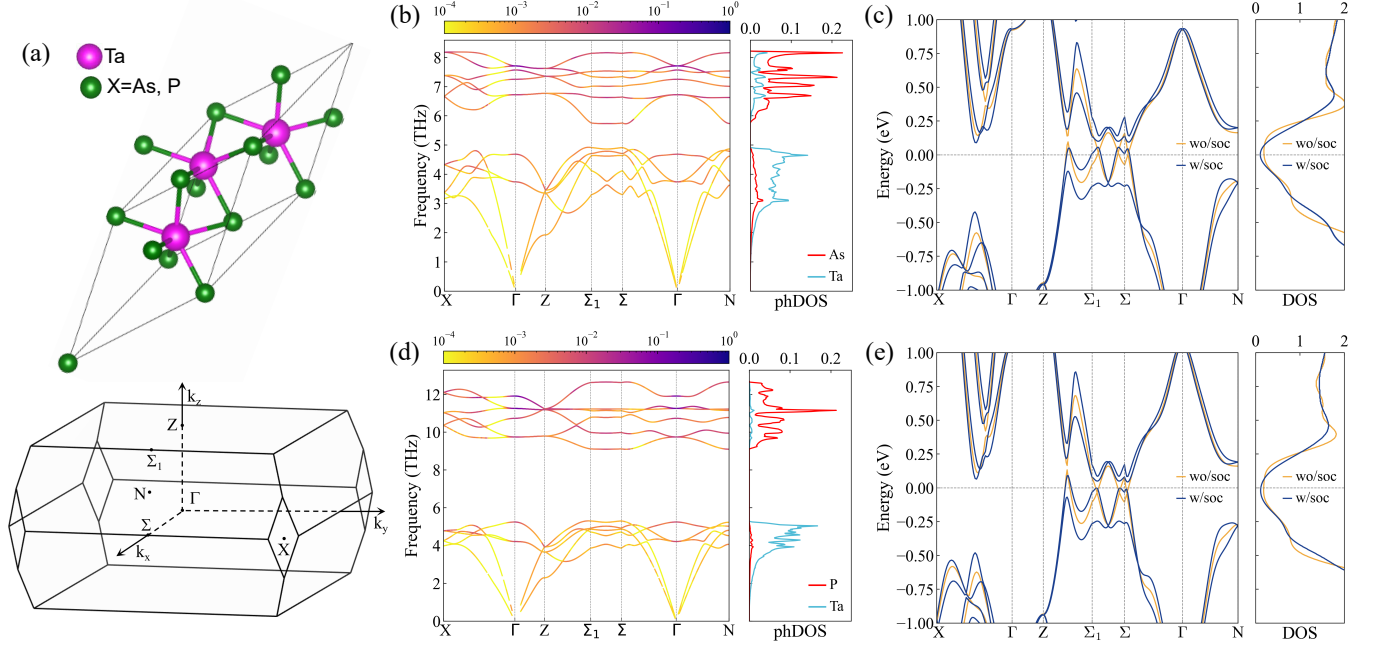


FIG. 1. (a) The primitive cell and Brillouin Zone of TaX ($\text{X} = \text{As}, \text{P}$). Phonon dispersion relation and projected phonon density of states (DOS) of (b) TaAs and (d) TaP , where the phonon linewidth due to ph-el scattering is projected onto the corresponding phonon structure. Electronic band structure and electronic DOS of (c) TaAs and (e) TaP without and with including spin-orbital coupling (SOC).

study of phonon and electron thermal conductivity in the Weyl semimetals TaAs and TaP . Our results reveal that heat conduction in both WSMs is dominated by phonons, challenging the conventional belief that κ_{ph} is negligible in metals. In TaP specifically, the calculated κ_{ph} reaches 171 W/mK along the a -axis and 82 W/mK along the c -axis at room temperature (RT), far surpassing its electronic counterpart of 33 W/mK and 11 W/mK, respectively. This exceptionally high κ_{ph} primarily originates from weak ph-el scattering, arising from the low electronic density of states near the Fermi level induced by the topological band structure. Additionally, the large κ_{ph} is partly due to weak phonon-phonon scattering, resulting from the combined effects of acoustic phonon bunching and a large a-o gap. Owing to the substantial phonon contribution, the derived Lorenz number deviates by more than an order of magnitude from the Sommerfeld value. These findings underscore the anomalous thermal transport behavior in topological semimetals.

In metals, the total κ comprises contributions from both phonons and electrons, i.e., $\kappa = \kappa_{\text{ph}} + \kappa_{\text{e}}$. The phonon thermal conductivity tensor $\kappa_{\text{ph}}^{\alpha\beta}$ is obtained by solving the linearized phonon Boltzmann transport equation (BTE), which can be expressed as

$$\kappa_{\text{ph}}^{\alpha\beta} = \sum_{pq} C_{pq} v_{pq}^\alpha \otimes F_{pq}^\beta \quad (1)$$

where p, q , C_{pq} , v_{pq}^α , and F_{pq}^β are the phonon branches, wave vector, mode-resolved heat capacity, phonon group

velocity, and mean free path, respectively, with α and β representing Cartesian axes. F_{pq} is limited by multiple scattering mechanisms, including 3ph ($1/\tau_{pq}^{3\text{ph}}$), four-phonon (4ph, $1/\tau_{pq}^{4\text{ph}}$), isotope (ph-iso, $1/\tau_{pq}^{\text{iso}}$), and ph-el ($1/\tau_{pq}^{\text{ph-el}}$) scattering processes. Detailed expressions for 3ph, 4ph, and iso can be found elsewhere [21, 31]. The ph-el scattering is obtained from the imaginary part of the phonon self-energy Π_{pq}'' [32], given by $1/\tau_{pq}^{\text{ph-el}} = 2\Pi_{pq}''/\hbar$, which can be directly obtained from the phonon linewidth computed using the EPW code [33].

The electrical conductivity (σ) and electronic thermal conductivity tensor (κ_e) can be obtained by solving the electron BTE, given as [34]

$$\sigma^{\alpha\beta} = \frac{2e^2}{N_{\mathbf{k}} V_0 k_B T} \sum_{n\mathbf{k}} f_{n\mathbf{k}}^0 (1 - f_{n\mathbf{k}}^0) \nu_{n\mathbf{k}}^\alpha \otimes \mathbf{F}_{n\mathbf{k}}^\beta, \quad (2)$$

$$\kappa_e^{\alpha\beta} = \frac{2}{N_{\mathbf{k}} V_0 k_B T^2} \sum_{n\mathbf{k}} f_{n\mathbf{k}}^0 (1 - f_{n\mathbf{k}}^0) \times (E_{n\mathbf{k}} - E_f)^2 \mathbf{v}_{n\mathbf{k}}^\alpha \otimes \mathbf{F}_{n\mathbf{k}}^\beta - T(\sigma^{\alpha\beta} S^{\alpha\beta})^2 / \sigma^{\alpha\beta}, \quad (3)$$

where e , k_B , n , \mathbf{k} , and $N_{\mathbf{k}}$ denote the elementary charge, Boltzmann constant, band index, wave vector, and the number of uniformly sampled \mathbf{k} points, respectively. $f_{n\mathbf{k}}^0$ is the equilibrium Fermi-Dirac distribution, and $\mathbf{v}_{n\mathbf{k}}^\alpha$ is the electron velocity. $\mathbf{F}_{n\mathbf{k}}^\beta = \nu_{n\mathbf{k}}^\beta \tau_{n\mathbf{k}}^{\text{el-ph}}$ is the electron

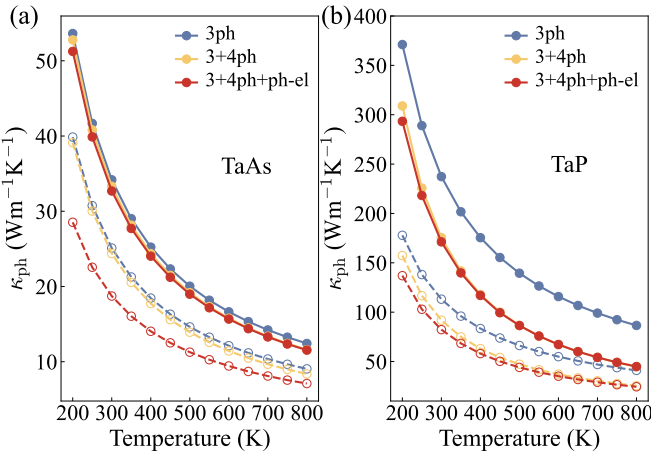


FIG. 2. Temperature-dependent κ_{ph} of (a) TaAs and (b) TaP with different combinations of scattering mechanisms. The filled and empty symbols correspond to the κ_{ph} along the a and c axes, respectively.

mean free path limited by the electron-phonon scattering (el-ph, $\tau_{nk}^{\text{el-ph}}$), which is accurately calculated by an iterative scheme. The el-ph coupling matrix elements are first computed on coarse grids of $12 \times 12 \times 12$ \mathbf{k} -points and $4 \times 4 \times 4$ \mathbf{q} -points, and subsequently interpolated onto dense $60 \times 60 \times 60$ \mathbf{k} - and \mathbf{q} -point grids using the maximally localized Wannier function basis as implemented in the EPW package [33]. The phonon thermal conductivity κ_{ph} is obtained by solving the phonon BTE with an iterative scheme using a modified version of Sheng-BTE code [35–38]. To compute the phonon-limited electronic transport properties, we further adopt fine grids of $80 \times 80 \times 80$ \mathbf{k} - and \mathbf{q} -points to evaluate the el-ph scattering rates and solve the electron BTE via the Perturbo code [39]. Further computational details are provided in the Supplement Materials (SM)[40].

TaAs and TaP both crystallize in a body-centered tetragonal structure with the space group $I4_1md$ (No. 109), with each primitive cell containing four atoms, as illustrated in Fig. 1(a). The optimized lattice parameters of TaAs (TaP) are $a = b = 3.456$ (3.329) Å and $c = 11.718$ (11.392) Å, in good agreement with earlier experimental and theoretical values [5, 6, 15, 41, 42]. Apparently, both compounds exhibit pronounced lattice anisotropy, which manifests in various physical properties, including electronic and thermal transport behavior. Figures 1 (b) and (d) present the phonon dispersions of TaAs and TaP along high-symmetry paths within the irreducible Brillouin zone (BZ), together with the projected phonon density of states (DOS). Substituting As with P shifts the overall phonon spectrum toward higher frequencies, a result of enhanced bond strength as reported previously [30]. More importantly, the increased anion–cation mass ratio in TaP leads to a wider a–o phonon frequency gap, which suppresses the 3ph scattering channels involving three acoustic phonons (aaa). As a result, a higher κ_{ph}

is expected in TaP than in TaAs.

The electronic band structures of TaAs and TaP with and without spin-orbit coupling (SOC) are shown in Figs. 1(c) and (e). In the absence of SOC, the valence and conduction bands of both compounds cross near the Fermi level, forming mirror-symmetry-protected closed nodal rings within the mirror plane [5]. Upon inclusion of SOC, these nodal rings become fully gapped along high-symmetry directions, with band degeneracy lifted everywhere except at isolated crossing points, giving rise to discrete Weyl nodes. This band topology evolution has been well documented in earlier studies [5, 43]. Due to the strong influence of band structure near the Fermi level on transport properties, the inherent SOC effects are explicitly taken into account in all subsequent calculations. Notably, the presence of Weyl nodes results in a extremely low electronic density of states (DOS) at the Fermi level, as shown in the right panels of Figs. 1(c) and (e). This feature implies intrinsically weak el-ph coupling in both materials, as the scattering strength is generally proportional to the electronic DOS at the Fermi level [22]. This is corroborated by the computed ph-el scattering rates projected onto the phonon dispersions (see Figs. 1(b) and (d)), which are rather low, especially for acoustic phonons, with rates below 0.01 ps^{-1} .

The κ_{ph} of TaAs and TaP are then predicted from 200 to 800 K by incorporating different scattering mechanisms. The results are shown in Fig. 2. Compared to the case considering only 3ph scattering, κ_{ph} of TaAs decreases only slightly over the entire temperature range when 4ph scattering is included. In contrast, κ_{ph} of TaP exhibits a significant reduction even at RT, with a drop of $\sim 26\%$. The markedly stronger effect of 4ph scattering in TaP is a direct consequence of its distinct phonon spectrum. Notably, when ph–el scattering is further included, κ_{ph} along the a -axis remains nearly unchanged in both WSMs. Along the c -axis, however, a pronounced reduction is observed. Specifically, κ_{ph} along the c -axis of TaAs decreases by about 23% at RT due to ph–el scattering. This anisotropic behavior is directly reflected in the path-dependent ph–el scattering rates shown in Figs. 1(b) and (d): the phonon linewidths from ph–el processes are considerably smaller for acoustic phonons along other paths than along the $\Gamma - \mathbf{Z}$ path, which corresponds to the c -axis. When all scattering mechanisms are taken into account, the predicted κ_{ph} of TaP along the a -axis at RT reaches 171 W/mK, which is substantially higher than that of TaAs (33 W/mK). This trend aligns with expectations: substituting As with P increases the phonon frequencies and widens the a–o gap, both known to enhance κ_{ph} [44, 45]. Additionally, we see that the κ_{ph} in both WSMs exhibits strong anisotropy due to the pronounced lattice anisotropy, with values along the a -axis being significantly higher than those along the c -axis.

To clarify the frequency ranges affected by different scattering mechanisms, we plot in Figs. 3(a) and (c) the spectral contributions to κ_{ph} along the a -axis for TaAs and TaP at RT. In both WSMs, the dominant contribu-

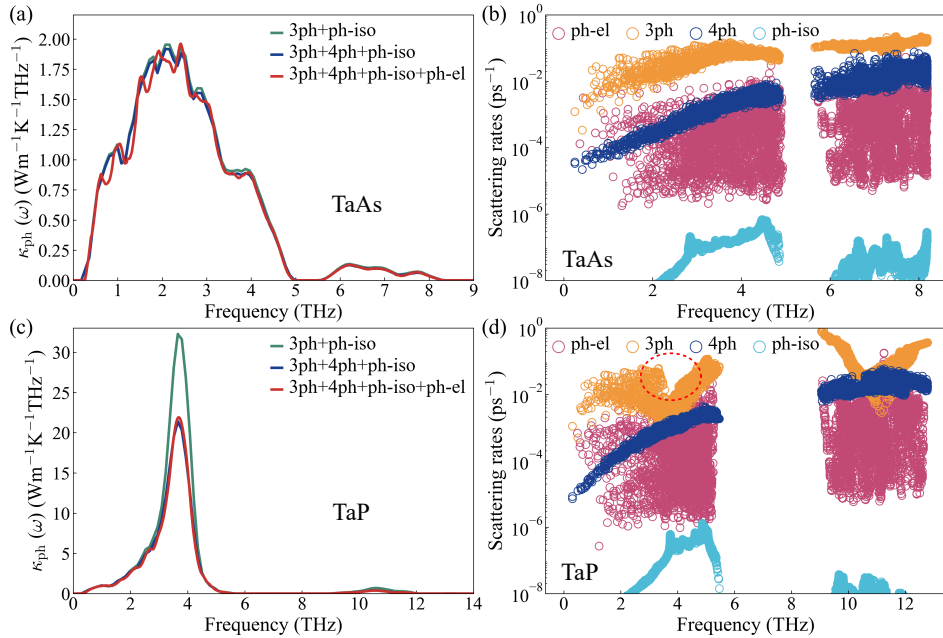


FIG. 3. Calculated spectral contributions to the κ_{ph} of (a) TaAs and (c) TaP along the *a*-axis at RT. The phonon scattering rates contributed from 3ph, 4ph, ph-iso, and ph-el processes for (b) TaAs and (d) TaP at RT.

tion to the total κ_{ph} originates from phonons with frequencies below 5 THz, corresponding to their acoustic modes. In TaAs, the contribution of these heat-carrying phonons to κ_{ph} is less influenced by both 4ph and ph-el scattering. As illustrated in Fig. 3(b), the 3ph scattering rates in this frequency regime surpass the 4ph and ph-el scattering rates by nearly two orders of magnitude.

In contrast, for TaP, Fig. 3(c) reveals that 4ph scattering significantly suppresses the contribution of phonons within 3-5 THz. This can be understood from Fig. 3(d), where the 3ph scattering rates exhibit a pronounced dip around 4 THz, as marked by the oval. This dip results from constraints imposed by the unique phononic structure including the large *a*-*o* gap and acoustic phonon bunching (Fig. 1(d)), which strongly impede scattering processes involving *aaa* and two acoustic phonons combining into one optical phonon (*aoa*) [46, 47]. As a result, within this frequency region, the 4ph scattering rates become comparable to the 3ph rates. Similar to TaAs, the ph-el scattering rates in TaP remain substantially lower than the 3ph counterparts, affirming their minor effect on κ_{ph} .

Having obtained the κ_{ph} for these two compounds, we now turn to their electronic transport properties. The computed phonon-limited electrical conductivity is displayed in Figs. 4(a) and (d). For TaAs, our predictions along the *a*-axis agree reasonably with available experimental data [51–53], validating the reliability of our approach. We further predict electronic thermal conductivities and compare them with the phonon contributions in Figs. 4(b) and (e). It is seen that the κ_{e} of both compounds exhibits typical metallic behavior, with

a weak temperature dependence. In TaAs, κ_{ph} along the *a*-axis significantly exceeds κ_{e} below 600 K, while along the *c*-axis it dominates thermal transport over the entire temperature range. For example, the κ_{ph} along the *a*- and *c*-axes reaches 33 and 19 W/mK at RT, respectively, whereas the corresponding κ_{e} is only 14 and 7 W/mK. This anomalously large phonon contribution is even more pronounced in TaP, where κ_{ph} dominates thermal transport along both axes over the whole temperature range, e.g., κ_{ph} along the *a*-axis (171 W/mK) is about five times larger than κ_{e} (33 W/mK) at RT. These findings clearly depart from the conventional view that phonon thermal transport is insignificant in metals.

The thermal conductivity of metals is commonly extracted from electrical conductivity measurements via the WFL; therefore, an accurate determination of the Lorenz number is crucial for correctly interpreting their transport behavior. The temperature-dependent Lorenz numbers for TaAs and TaP are presented in Figs. 4(c) and (f), respectively. Considering only the electronic contribution κ_{e} , the derived Lorenz number $L_{\text{e}} = \kappa_{\text{e}}/(\sigma T)$ for TaP aligns well with the Sommerfeld value L_0 , whereas for TaAs it falls notably below L_0 at lower temperatures. This deviation has been broadly seen in metals and can be attributed to the distinct effects of inelastic el-ph scattering on heat and charge transport [29, 54]. Surprisingly, when the κ_{ph} is added, the resulting L for both compounds exhibits pronounced deviations from L_0 , particularly at lower temperatures. Specifically, the anomalously large κ_{ph} increases the *c*-axis L of TaAs by more than three times relative to L_0 near RT, while that of TaP even exceeds L_0 by over an order of magnitude.

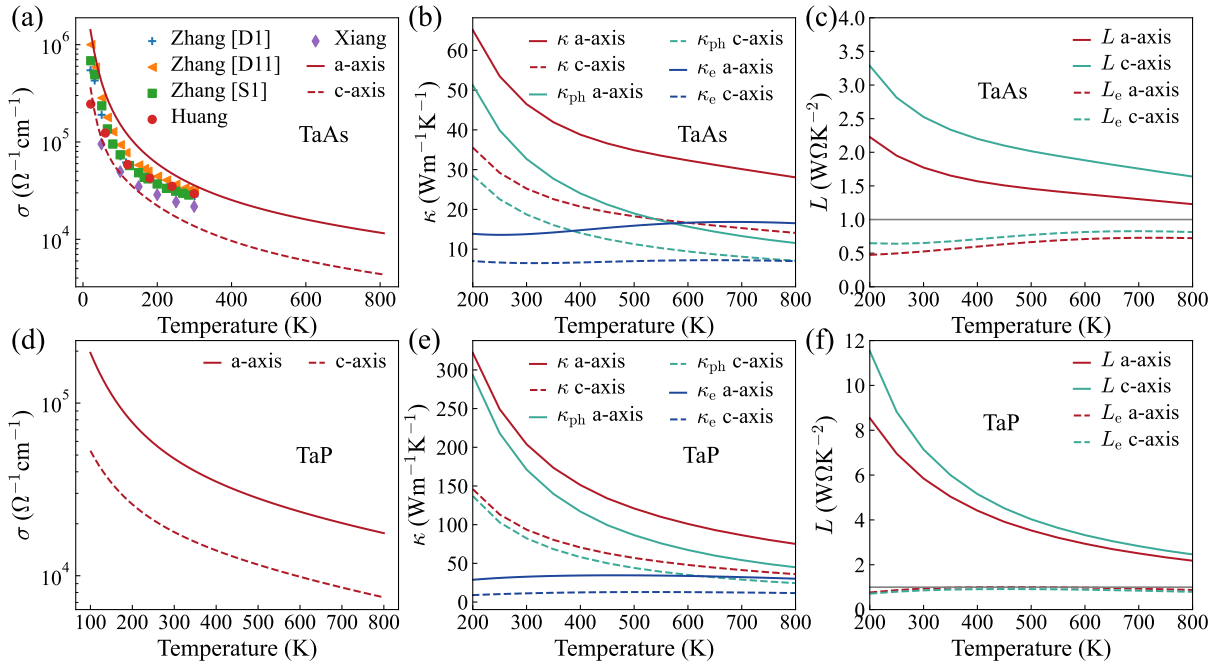


FIG. 4. (a, d) The electronic conductivity, (b, e) the κ_e , κ_{ph} , and total thermal conductivity ($\kappa = \kappa_{\text{ph}} + \kappa_e$), and (c, f) the Lorenz number as a function of temperature for TaAs and TaP, respectively.

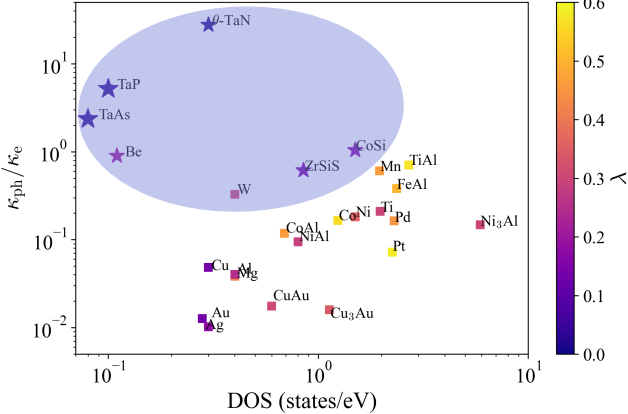


FIG. 5. The relative importance of κ_{ph} , as gauged by the ratio $\kappa_{\text{ph}}/\kappa_e$, for available topological semimetals and metals; the colorbar represents the corresponding el-ph coupling strength (λ). The presented data for the electronic DOS, κ_{ph} , κ_e , and λ are extracted from Refs. [22, 29, 48] and the Material Project database [49, 50]. Topological semimetals are marked with stars.

The above results highlight the unusually phonon-dominated thermal transport in TaAs and TaP, which makes the conventional WFL inadequate for describing their coupled thermal and electrical transport. It should be emphasized that such anomalous thermal behavior is not limited to these two compounds, but is expected to be universal across many other topological semimetals. This can be attributed to their unique electronic band struc-

ture, which leads to a small electronic density of states at the Fermi level (N_F), resulting in weak ph-el scattering and consequently a relatively large phonon contribution to thermal conductivity. To illustrate this point, Fig. 5 summarizes the ratio of κ_{ph} to κ_e as a function of N_F for reported topological semimetals [5, 23, 48, 55, 56], benchmarked against available data for conventional metals at RT [27, 29]. Evidently, topological semimetals generally exhibit a notably low N_F , which typically corresponds to a weak el-ph coupling strength (λ) [57]. As a result, the $\kappa_{\text{ph}}/\kappa_e$ ratio in topological semimetals is generally much higher than that in conventional metals, particularly in the cases of $\theta\text{-TaN}$ and the TaP reported in our study.

In summary, we have performed first-principles calculations for the electrical and thermal conductivities of TaAs and TaP based on the accurate solution of BTE. The results unveil a strikingly large phonon contribution to the total thermal conductivity compared to conventional metals, which leads to a significant deviation of the Lorenz number. Intriguingly, we predict that the κ_{ph} of TaP along the a -axis can reach 171 W/mK at RT, exceeding its electronic thermal conductivity by more than a factor of five. This large κ_{ph} stems from the synergistic effects of weak ph-el and 3ph scattering, arising from the unique electronic and phononic band structures, including fully gapped nodal rings near the Fermi level, and a large a - ω gap and acoustic bunching in the phonon spectrum. By extending our analysis to several representative systems, we further establish that phonon-mediated heat transport is a distinctive hallmark of the broader material family of topological semimetals. These find-

ings suggest that topological semimetals host intrinsic physical mechanisms capable of achieving high thermal conductivity, which warrants further theoretical and experimental studies on thermal transport in this class of materials.

I. ACKNOWLEDGEMENT

This work was supported by the National Natural Science Foundation of China (NSFC) (Grant No. 12374038), the Fundamental Research Fund for the Central Universities (Grant No. 2025CDJ-IAISYB-035), and the New Chongqing Youth Innovative Tal-

ent Project (Grant No. CSTB2025YITP-QCRCX006), the Major Science and Technology Project of the Chongqing Municipal Education Commission (Grant No. KJZD-M202500504), and the Chongqing Natural Science Foundation-Innovation and Development Joint Fund (Key Program) (Grant No. CSTB2023NSCQ-LZX0138). This work was supported in part by the NSFC (Grant Nos. 12404045, 52371148, 12547101), the Chongqing Natural Science Foundation (No. CSTB2025NSCQ-GPX1028), the Science and Technology Research Program of Chongqing Municipal Education Commission (No. KJZD-K202500512, No. KJQN-202400553), and the Foundation of Chongqing Normal University (No. 25XLB024 and No. 23XLB015).

[1] X. Wan, A. M. Turner, A. Vishwanath, and S. Y. Savrasov, Topological semimetal and fermi-arc surface states in the electronic structure of pyrochlore iridates, *Phys. Rev. B* **83**, 205101 (2011).

[2] B. Yan and C. Felser, Topological materials: Weyl semimetals, *Annu. Rev. Condens. Matter Phys.* **8**, 337 (2017).

[3] N. P. Armitage, E. J. Mele, and A. Vishwanath, Weyl and dirac semimetals in three-dimensional solids, *Rev. Mod. Phys.* **90**, 015001 (2018).

[4] N. Ong and S. Liang, Experimental signatures of the chiral anomaly in dirac–weyl semimetals, *Nat. Rev. Phys.* **3**, 394 (2021).

[5] H. Weng, C. Fang, Z. Fang, B. A. Bernevig, and X. Dai, Weyl semimetal phase in noncentrosymmetric transition-metal monophosphides, *Phys. Rev. X* **5**, 011029 (2015).

[6] B. Q. Lv, H. M. Weng, B. B. Fu, X. P. Wang, H. Miao, J. Ma, P. Richard, X. C. Huang, L. X. Zhao, G. F. Chen, Z. Fang, X. Dai, T. Qian, and H. Ding, Experimental discovery of weyl semimetal taas, *Phys. Rev. X* **5**, 031013 (2015).

[7] L. Yang, Z. Liu, Y. Sun, H. Peng, H. Yang, T. Zhang, B. Zhou, Y. Zhang, Y. Guo, M. Rahn, *et al.*, Weyl semimetal phase in the non-centrosymmetric compound taas, *Nat. Phys.* **11**, 728 (2015).

[8] S.-Y. Xu, C. Liu, S. K. Kushwaha, R. Sankar, J. W. Krizan, I. Belopolski, M. Neupane, G. Bian, N. Alidoust, T.-R. Chang, H.-T. Jeng, C.-Y. Huang, W.-F. Tsai, H. Lin, P. P. Shibayev, F.-C. Chou, R. J. Cava, and M. Z. Hasan, Observation of fermi arc surface states in a topological metal, *Science* **347**, 294 (2015).

[9] Y. Sun, S.-C. Wu, and B. Yan, Topological surface states and fermi arcs of the noncentrosymmetric weyl semimetals taas, tap, nbas, and nbp, *Phys. Rev. B* **92**, 115428 (2015).

[10] C. Shekhar, A. K. Nayak, Y. Sun, M. Schmidt, M. Nicklas, I. Leermakers, U. Zeitler, Y. Skourski, J. Wosnitza, Z. Liu, *et al.*, Extremely large magnetoresistance and ultrahigh mobility in the topological weyl semimetal candidate nbp, *Nat. Phys.* **11**, 645 (2015).

[11] C. Shekhar, F. Arnold, S.-C. Wu, Y. Sun, M. Schmidt, N. Kumar, A. G. Grushin, J. H. Bardarson, R. D. dos Reis, M. Naumann, *et al.*, Large and unsaturated negative magnetoresistance induced by the chiral anomaly in the weyl semimetal tap, *Preprint at <http://arxiv.org/abs/1506.06577>* (2015).

[12] J. Du, H. Wang, Q. Chen, Q. Mao, R. Khan, B. Xu, Y. Zhou, Y. Zhang, J. Yang, B. Chen, *et al.*, Large unsaturated positive and negative magnetoresistance in weyl semimetal tap, *Sci. China Phys. Mech. Astron.* **59**, 657406 (2016).

[13] C.-L. Zhang, C. Wang, Z. Yuan, X. Xu, G. Wang, C.-C. Lee, L. Pi, C. Xi, H. Lin, N. Harrison, *et al.*, Non-saturating quantum magnetization in weyl semimetal taas, *Nat. Commun.* **10**, 1028 (2019).

[14] F. Arnold, C. Shekhar, S.-C. Wu, Y. Sun, R. D. Dos Reis, N. Kumar, M. Naumann, M. O. Ajeesh, M. Schmidt, A. G. Grushin, *et al.*, Negative magnetoresistance without well-defined chirality in the weyl semimetal tap, *Nat. Commun.* **7**, 11615 (2016).

[15] X. Huang, L. Zhao, Y. Long, P. Wang, D. Chen, Z. Yang, H. Liang, M. Xue, H. Weng, Z. Fang, X. Dai, and G. Chen, Observation of the chiral-anomaly-induced negative magnetoresistance in 3d weyl semimetal taas, *Phys. Rev. X* **5**, 031023 (2015).

[16] Y. Li, Z. Wang, P. Li, X. Yang, Z. Shen, F. Sheng, X. Li, Y. Lu, Y. Zheng, and Z.-A. Xu, Negative magnetoresistance in weyl semimetals nbas and nbp: Intrinsic chiral anomaly and extrinsic effects, *Front. Phys.* **12**, 127205 (2017).

[17] P. E. C. Ashby and J. P. Carbotte, Chiral anomaly and optical absorption in weyl semimetals, *Phys. Rev. B* **89**, 245121 (2014).

[18] S. Jia, S.-Y. Xu, and M. Z. Hasan, Weyl semimetals, fermi arcs and chiral anomalies, *Nat. Mater.* **15**, 1140 (2016).

[19] X. Yuan, C. Zhang, Y. Zhang, Z. Yan, T. Lyu, M. Zhang, Z. Li, C. Song, M. Zhao, P. Leng, *et al.*, The discovery of dynamic chiral anomaly in a weyl semimetal nbas, *Nat. Commun.* **11**, 1259 (2020).

[20] B. Xu, Y. M. Dai, L. X. Zhao, K. Wang, R. Yang, W. Zhang, J. Y. Liu, H. Xiao, G. F. Chen, A. J. Taylor, D. A. Yarotski, R. P. Prasankumar, and X. G. Qiu, Optical spectroscopy of the weyl semimetal taas, *Phys. Rev. B* **93**, 121110 (2016).

[21] X. Ding, X. Jin, Z. Chang, D. Li, X. Zhou, X. Yang, and R. Wang, Anharmonicity-induced phonon hardening and anomalous thermal transport in sczn, *Phys. Rev. B* **110**,

054304 (2024).

[22] A. Kundu, X. Yang, J. Ma, T. Feng, J. Carrete, X. Ruan, G. K. H. Madsen, and W. Li, Ultrahigh thermal conductivity of θ -phase tantalum nitride, *Phys. Rev. Lett.* **126**, 115901 (2021).

[23] X. Jin, Q. Zhang, D. Li, Z. Cheng, J. Wang, X. Lv, X. Zhou, R. Wang, X. Ding, P. Yu, and X. Yang, Anharmonicity-driven avoided phonon crossing and anomalous thermal transport in the nodal-line semimetal zrsis, *Phys. Rev. B* **112**, 184311 (2025).

[24] G. V. Chester and A. Thellung, The law of wiedemann and franz, *Proc. Phys. Soc* **77**, 1005 (1961).

[25] R. Makinson, The thermal conductivity of metals, in *Mathematical Proceedings of the Cambridge Philosophical Society*, Vol. 34 (Cambridge University Press, 1938) pp. 474–497.

[26] P. G. Klemens and R. K. Williams, Thermal conductivity of metals and alloys, *Int. Mater. Rev.* **31**, 197 (1986), <https://doi.org/10.1179/imtr.1986.31.1.197>.

[27] Y. Chen, J. Ma, and W. Li, Understanding the thermal conductivity and lorenz number in tungsten from first principles, *Phys. Rev. B* **99**, 020305 (2019).

[28] Y. Chen, G. Pang, F. Meng, and W. Li, Origin of the high lattice thermal conductivity of beryllium among the elemental metals, *Phys. Rev. B* **109**, L220302 (2024).

[29] Z. Tong, S. Li, X. Ruan, and H. Bao, Comprehensive first-principles analysis of phonon thermal conductivity and electron-phonon coupling in different metals, *Phys. Rev. B* **100**, 144306 (2019).

[30] X. Ding, X. Jin, D. Li, J. Fan, X. Zhou, X. Lv, X. Yang, Z. Cheng, and R. Wang, Concurrent high thermal conductivity and high carrier mobility in tetragonal tantalum nitride, *Appl. Phys. Rev.* **12**, 021419 (2025).

[31] L. Wei, X. Jin, Z. Zhou, X. Yang, G. Wang, and X. Zhou, Tensile strain induced enhancement of lattice thermal conductivity and its origin in two-dimensional snc, *Phys. Rev. B* **110**, 045406 (2024).

[32] C. Li, N. K. Ravichandran, L. Lindsay, and D. Broido, Fermi surface nesting and phonon frequency gap drive anomalous thermal transport, *Phys. Rev. Lett.* **121**, 175901 (2018).

[33] S. Poncé, E. Margine, C. Verdi, and F. Giustino, Epw: Electron–phonon coupling, transport and superconducting properties using maximally localized wannier functions, *Comput. Phys. Commun.* **209**, 116 (2016).

[34] W. Li, Electrical transport limited by electron-phonon coupling from boltzmann transport equation: An ab initio study of si, al, and mos₂, *Phys. Rev. B* **92**, 075405 (2015).

[35] W. Li, J. Carrete, N. A. Katcho, and N. Mingo, Shengbte: A solver of the boltzmann transport equation for phonons, *Comput. Phys. Commun.* **185**, 1747 (2014).

[36] Z. Han, X. Yang, W. Li, T. Feng, and X. Ruan, Four-phonon: An extension module to shengbte for computing four-phonon scattering rates and thermal conductivity, *Comput. Phys. Commun.* **270**, 108179 (2022).

[37] X. Yang, A. Jena, F. Meng, S. Wen, J. Ma, X. Li, and W. Li, Indirect electron-phonon interaction leading to significant reduction of thermal conductivity in graphene, *Mat. Today Phys.* **18**, 100315 (2021).

[38] X. Yang, Z. Liu, F. Meng, and W. Li, Tuning the phonon transport in bilayer graphene to an anomalous regime dominated by electron-phonon scattering, *Phys. Rev. B* **104**, L100306 (2021).

[39] J.-J. Zhou, J. Park, I.-T. Lu, I. Maliyov, X. Tong, and M. Bernardi, Perturbo: A software package for ab initio electron–phonon interactions, charge transport and ultrafast dynamics, *Comput. Phys. Commun.* **264**, 107970 (2021).

[40] See supplemental material for the computational details, convergence tests, and supplment figures, which include Refs. [33, 35, 39, 58–62].

[41] B. Lv, N. Xu, H. Weng, J. Ma, P. Richard, X. Huang, L. Zhao, G. Chen, C. Matt, F. Bisti, *et al.*, Observation of weyl nodes in taas, *Nat. Phys.* **11**, 724 (2015).

[42] Z. Liu, S. B. Mishra, J.-M. Lihm, S. Poncé, and E. R. Margine, Phonon-limited carrier transport in the weyl semimetal taas, *Phys. Rev. B* **112**, 104311 (2025).

[43] C.-C. Lee, S.-Y. Xu, S.-M. Huang, D. S. Sanchez, I. Bełopolski, G. Chang, G. Bian, N. Alidoust, H. Zheng, M. Neupane, B. Wang, A. Bansil, M. Z. Hasan, and H. Lin, Fermi surface interconnectivity and topology in weyl fermion semimetals taas, tap, nbas, and nbp, *Phys. Rev. B* **92**, 235104 (2015).

[44] G. Slack, Nonmetallic crystals with high thermal conductivity, *J. Phys. Chem. Solids* **34**, 321 (1973).

[45] L. Lindsay, D. A. Broido, and T. L. Reinecke, First-principles determination of ultrahigh thermal conductivity of boron arsenide: A competitor for diamond?, *Phys. Rev. Lett.* **111**, 025901 (2013).

[46] K. Chen, X. Jin, and X. Yang, Symmetry-breaking strain drives significant reduction in lattice thermal conductivity: A case study of boron arsenide, *Chin. Phys. Lett.* **42**, 120801 (2025).

[47] T. Wang, X. Li, Z. Ju, G. Zhang, D. Ma, W. Li, and L. Zhang, Atomic mass engineering of ultra-high thermal conductivity in large bandgap materials: A case study with boron arsenide, *Chin. Phys. Lett.* **42**, 070802 (2025).

[48] R. Li, J. Li, L. Wang, J. Liu, H. Ma, H.-F. Song, D. Li, Y. Li, and X.-Q. Chen, Underlying topological dirac nodal line mechanism of the anomalously large electron-phonon coupling strength on a be (0001) surface, *Phys. Rev. Lett.* **123**, 136802 (2019).

[49] A. Jain, S. P. Ong, G. Hautier, W. Chen, W. D. Richards, S. Dacek, S. Cholia, D. Gunter, D. Skinner, G. Ceder, and K. A. Persson, Commentary: The materials project: A materials genome approach to accelerating materials innovation, *APL Materials* **1**, 011002 (2013).

[50] J. M. Munro, K. Latimer, M. K. Horton, S. Dwaraknath, and K. A. Persson, An improved symmetry-based approach to reciprocal space path selection in band structure calculations, *npj Computational Materials* **6**, 112 (2020).

[51] W. Witczak-Krempa and Y. B. Kim, Topological and magnetic phases of interacting electrons in the pyrochlore iridates, *Phys. Rev. B* **85**, 045124 (2012).

[52] C.-L. Zhang, Z. Yuan, Q.-D. Jiang, B. Tong, C. Zhang, X. C. Xie, and S. Jia, Electron scattering in tantalum monoarsenide, *Phys. Rev. B* **95**, 085202 (2017).

[53] J. Xiang, S. Hu, M. Lv, J. Zhang, H. Zhao, G. Chen, W. Li, Z. Chen, and P. Sun, Anisotropic thermal and electrical transport of weyl semimetal taas, *J. Phys. Condens. Matter* **29**, 485501 (2017).

[54] F. Sun, S. Mishra, U. Stockert, R. Daou, N. Kikugawa, R. S. Perry, E. Hassinger, S. A. Hartnoll, A. P. Mackenzie, and V. Sunko, The lorenz ratio as a guide to scattering contributions to transport in strongly correlated metals, *Proc. Natl. Acad. Sci.* **121**, e2318159121 (2024),

<https://www.pnas.org/doi/pdf/10.1073/pnas.2318159121>.

[55] H. Weng, C. Fang, Z. Fang, and X. Dai, Topological semimetals with triply degenerate nodal points in θ -phase tantalum nitride, *Phys. Rev. B* **93**, 241202 (2016).

[56] Z. Rao, H. Li, T. Zhang, S. Tian, C. Li, B. Fu, C. Tang, L. Wang, Z. Li, W. Fan, *et al.*, Observation of unconventional chiral fermions with long fermi arcs in cosi, *Nature* **567**, 496 (2019).

[57] X. Yao, Y. Xun, Z. Zhu, S. Zhao, and W. Li, Origin of the high electrical conductivity of the delafossite metal pdco_2 , *Phys. Rev. B* **109**, 075110 (2024).

[58] G. Kresse and J. Hafner, Ab initio molecular dynamics for open-shell transition metals, *Phys. Rev. B* **48**, 13115 (1993).

[59] G. Kresse and J. Furthmüller, Efficient iterative schemes for ab initio total-energy calculations using a plane-wave basis set, *Phys. Rev. B* **54**, 11169 (1996).

[60] P. E. Blöchl, Projector augmented-wave method, *Phys. Rev. B* **50**, 17953 (1994).

[61] J. P. Perdew, K. Burke, and M. Ernzerhof, Generalized gradient approximation made simple, *Phys. Rev. Lett.* **77**, 3865 (1996).

[62] P. Giannozzi, S. Baroni, N. Bonini, M. Calandra, R. Car, C. Cavazzoni, D. Ceresoli, G. L. Chiarotti, M. Cococcioni, I. Dabo, A. Dal Corso, S. de Gironcoli, S. Fabris, G. Fratesi, R. Gebauer, U. Gerstmann, C. Gougaussis, A. Kokalj, M. Lazzeri, L. Martin-Samos, N. Marzari, F. Mauri, R. Mazzarello, S. Paolini, A. Pasquarello, L. Paulatto, C. Sbraccia, S. Scandolo, G. Sclauzero, A. P. Seitsonen, A. Smogunov, P. Umari, and R. M. Wentzcovitch, Quantum espresso: a modular and open-source software project for quantum simulations of materials, *J. Phys. Condens. Matter* **21**, 395502 (2009).